

RADAR IMAGING AND PHYSICAL CHARACTERIZATION OF NEAR-EARTH ASTEROID (162421) 2000 ET70

S. P. NAIDU¹, J. L. MARGOT^{1,2}, M. W. BUSCH^{1,6}, P. A. TAYLOR³, M. C. NOLAN³, E. S. HOWELL³, M. BROZOVIC⁴,
L. A. M. BENNER⁴, J. D. GIORGINI⁴, C. MAGRI⁵

(Dated:)
Draft version January 25, 2013

ABSTRACT

We observed near-Earth asteroid (162421) 2000 ET70 using the Arecibo and Goldstone radar systems over a period of 12 days during its close approach to the Earth in February 2012. We obtained continuous wave spectra and range-Doppler images with range resolutions as fine as 15 m. Inversion of the radar images yields a detailed shape model with an effective resolution of 100 m. The asteroid has overall dimensions of 2.6 km \times 2.2 km \times 2.1 km and a surface rich with kilometer-scale ridges and concavities. It is a principal axis rotator and spins in a retrograde manner with a spin period of 8.96 ± 0.02 hours. In terms of gravitational slopes evaluated at scales of 100 m, the surface seems mostly relaxed with over 99% of the surface having slopes less than 30° , but there are some outcrops at the north pole that may have steeper slopes. Our precise measurements of the range and velocity of the asteroid, combined with optical astrometry, enables reliable trajectory predictions for this potentially hazardous asteroid in the interval 460-2813.

Subject headings: Near-Earth objects; Asteroids; Radar observations; Orbit determination

1. INTRODUCTION

Radar astronomy is arguably the most powerful Earth-based technique for characterizing the physical properties of near-Earth asteroids (NEAs). Radar observations routinely provide images with decameter spatial resolution. These images can be used to obtain accurate astrometry, model shapes, measure near-surface radar scattering properties, and investigate many other physical properties (e.g. sizes, spin states, masses, densities). Radar observations have led to the discovery of asteroids exhibiting non-principal axis rotation (e.g., Ostro et al. 1995; Benner et al. 2002), binary and triple NEAs (e.g., Margot et al. 2002; Ostro et al. 2006; Shepard et al. 2006; Nolan et al. 2008; Brozović et al. 2011), and contact binary asteroids (e.g., Hudson and Ostro 1994; Benner et al. 2006; Brozovic et al. 2010). Radar-derived shapes and spins have been used to investigate various physical processes (Yarkovsky, YORP, BYORP, tides, librations, etc.) that are important to the evolution of NEAs (e.g., Chesley et al. 2003; Nugent et al. 2012; Lowry et al. 2007; Taylor et al. 2007; Ostro et al. 2006; Scheeres et al. 2006; Taylor and Margot 2011; Fang et al. 2011; Fang and Margot 2012).

Here we present the radar observations and detailed physical characterization of NEA (162421) 2000 ET70. This Aten asteroid ($a=0.947$ AU, $e=0.124$, $i=22.3^\circ$) was discovered on March 8, 2000 by the Lincoln Near-Earth

Asteroid Research (LINEAR) program in Socorro, New Mexico. Its absolute magnitude was reported to be 18.2 (Whiteley 2001) which, taken at face value, suggests a diameter between 0.5 and 1.5 km (assuming an optical albedo between 0.4 and 0.04). Alvarez et al. (2012) obtained a lightcurve of the asteroid during its close approach to the Earth in February 2012. They reported a lightcurve period of 8.947 ± 0.001 hours and a lightcurve amplitude of 0.60 ± 0.07 . Whiteley (2001) classified 2000 ET70 as an X-type asteroid which is a degenerate group of asteroids consisting of E, M, and P classes (Tholen 1984). Mike Hicks (personal communication) indicated that his observations were best matched by a C-type or possibly E-type. One of us (EH) classified it as Xk in the taxonomic system of Bus-DeMeo (DeMeo et al. 2009).

2. OBSERVATIONS AND DATA PROCESSING

We observed 2000 ET70 from February 12, 2012 to February 17, 2012 using the Arecibo S-band (2380 MHz, 13 cm) radar and from February 15, 2012 to February 23, 2012 using the Goldstone X-band (8560 MHz, 3.5 cm) radar. The asteroid moved ~ 74 degrees across the sky during this time and it came closest to Earth on February 19 at a distance of ~ 0.045 Astronomical Units (AU) (Fig. 1). We observed it again in August 2012 when it made another close approach to Earth at a distance of ~ 0.15 AU.

Radar observing involved transmitting a radio wave for approximately the round-trip light-time (RTT) to the asteroid, ~ 45 seconds at closest approach, and then receiving the echo reflected back from the target for a comparable duration. Each transmit-receive cycle is called a *run*. On each day we carried out runs with a monochromatic continuous wave (CW) to obtain Doppler spectra, followed by runs with a modulated carrier to obtain range-Doppler images. Table 1 summarizes the CW and range-Doppler imaging runs.

¹ Department of Earth and Space Sciences, University of California, Los Angeles, CA 90095, USA

² Department of Physics and Astronomy, University of California, Los Angeles, CA 90095, USA

³ Arecibo Observatory, HC3 Box 53995, Arecibo, PR 00612, USA

⁴ Jet Propulsion Laboratory, California Institute of Technology, Pasadena, CA 91109-8099, USA

⁵ University of Maine at Farmington, 173 High Street, Preble Hall, Farmington, ME 04938, USA

⁶ Now at National Radio Astronomy Observatory, 1003 Lopezville Road, Socorro, NM 87801, USA

TABLE 1
RADAR OBSERVATIONS OF (162421) 2000 ET70

Tel	UT Date yyyy-mm-dd	MJD	Eph	RTT (s)	PTX (kW)	δr (m)	δf (Hz)	Code	Start-Stop hhmmss-hhmmss	Runs
A	2012-02-12	55969	s41	69	828	cw	0.167	none	082751-083755	5
			s41			15	0.075	65535	084247-102947	48
			s41			15	0.075	8191	105318-110955	8
A	2012-02-13	55970	s41	64	860	cw	0.182	none	081106-082308	6
			s43			15	0.075	65535	083034-105326	54
A	2012-02-14	55971	s43	60	811	cw	0.196	none	075956-080443	3
			s43			15	0.075	65535	080640-101945	59
A	2012-02-15	55972	s43	56	785	cw	0.213	none	074302-074729	3
			s43			15	0.075	65535	080301-080918	4
			s47			15	0.075	65535	081638-093235	42
			s47			15	0.075	65535	093749-100946	18
G	2012-02-15	55972	s43	56	420	cw		none	085515-090327	5
			s43			75	1.532	255	091748-093320	9
			s45			37.5		255	094624-115924	73
			s45			37.5		255	094624-115924	5
A	2012-02-16	55973	s51	52	760	cw	0.227	none	073418-073830	3
			s49			15	0.075	65535	074056-074652	4
									074838-075106	2
			s49			15	0.075	65535	075328-093816	62
G	2012-02-16	55973	s49	52	420	cw		none	091546-092330	5
			s49			75	1.532	512	095639-100239	4
			s49			37.5	0.488	none	113521-114633	7*
			s49			15	1.0	none	121554-124710	18*
			s49			15	1.0	none	131001-132809	11*
			s49			15	1.0	none	132904-152931	70*
A	2012-02-17	55974	s53	49	775	cw	0.244	none	073800-074157	3
			s53			15	0.075	65535	074436-084859	40
G	2012-02-17	55974	s53	49	420	cw		none	070553-071310	5
			s53			75	1.532	512	074255-080001	11
			s53			37.5	0.977	none	081657-122419	152*
G	2012-02-18	55975	s53	47	420	cw		none	070551-071250	5
			s53			75	1.532	512	073604-075052	10
			s53			37.5	0.977	none	080115-083144	20*
			s53			37.5	0.977	none	083651-084524	6*
G	2012-02-19	55976	s55	46	420	cw		none	070551-071241	5
			s55			75	1.532	512	072155-973625	10
			s55			37.5	0.977	none	074612-111358	136*
			s55			37.5	0.977	none	114410-130706	55*
G	2012-02-20	55977	s57	45	420	cw		none	071051-071742	5
			s57			37.5	0.977	none	103149-113359	41*
			s57			37.5	0.977	none	121608-121954	3*
G	2012-02-22	55979	s59	48	420	cw		none	094825-095542	5
			s59			75	0.957	512	100253-102135	12
			s59			37.5	0.977	none	103251-103514	2*
			s59			37.5	0.977	none	103606-104502	6*
G	2012-02-23	55980	s59	50	420	cw		none	083310-084053	5
			s59			75	0.957	512	084948-090941	12
			s59			37.5	0.977	none	092046-105520	55*
A	2012-08-24	56163	s72	153	721	cw		none	151051-151825	2
									154651-163117	9
						2	2	8191	163659-174101	13
A	2012-08-26	56165	s72	157	722	cw		none	150424-162038	15

NOTE. — The first column indicates the telescope: Arecibo (A) or Goldstone (G). MJD is the modified Julian date of the observation. Eph is the ephemeris solution number used (Section 3). RTT is the round-trip light-time to the target. PTX is the transmitter power. δr and δf are the range and Doppler resolutions, respectively, of the processed data. Code is the length of the pseudo-random code used. The timespan of the received data are listed by their UT start and stop times. Runs is the number of transmit-receive cycles during the timespan. An asterisk (*) indicates chirp runs.

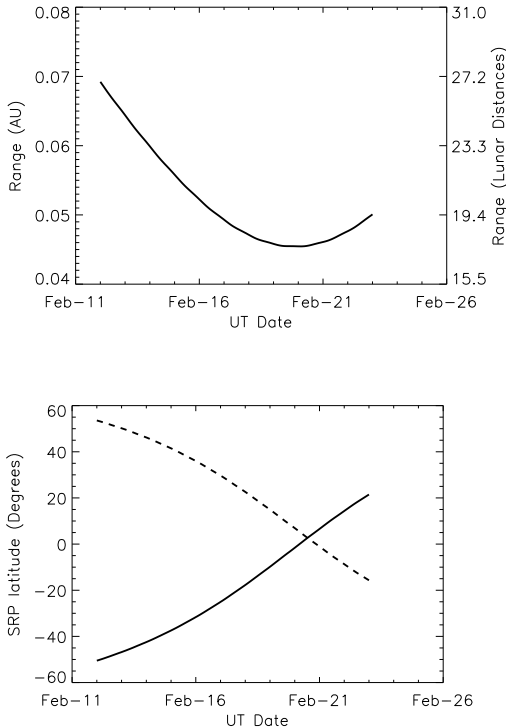


FIG. 1.— Distance of 2000 ET70 from Earth (top) and sub-radar point (SRP) latitude (bottom) during the primary observing period. Solid and dashed lines in the bottom panel show SRP latitude for the prograde and retrograde spin vectors, respectively (Section 6).

For CW runs a carrier wave at a fixed frequency was transmitted for the RTT to the asteroid. The received echo from the asteroid was demodulated, sampled, and recorded. A fast Fourier transform (FFT) was applied to each echo timeseries to obtain the CW spectra. The total frequency extent (Δf) or bandwidth (BW) of the CW spectra is equal to the sampling frequency (f_s) or the reciprocal of the sampling period (P_s):

$$\Delta f = f_s = \frac{1}{P_s}. \quad (1)$$

The spectral resolution (δf) is given by:

$$\delta f = \frac{\Delta f}{n}, \quad (2)$$

where n is the FFT length. Finer spectral resolution can be achieved by increasing n , however the signal-to-noise ratio (SNR) in each frequency bin decreases as $1/\sqrt{n}$. The finest possible resolution that can be achieved is limited by the number of samples obtained in one run. If we were recording for the full duration of the RTT, the number of samples obtained in one run would be $n = \text{RTT} \times f_s$, and the resolution would be $\delta f = 1/\text{RTT}$. In reality we cannot transmit for a full RTT as it takes several seconds to switch between transmission and reception, so the finest possible resolution is $\delta f = 1/(\text{RTT} - t_{\text{switch}})$, where t_{switch} is the switching time.

For range-Doppler imaging two different *pulse compression* techniques were used to achieve fine range reso-

lution while maintaining adequate SNR (Peebles 2007). Pulse compression is a signal conditioning and processing technique used in radar systems to achieve a high range resolution without severely compromising the ability to detect or image the target. The range resolution achievable by a radar is proportional to the pulse duration, or, equivalently, inversely proportional to the effective bandwidth of the transmitted signal. However, decreasing the pulse duration reduces the total transmitted energy per pulse and hence it negatively affects the ability to detect the radar target. Pulse compression techniques allow for the transmission of a long pulse while still achieving the resolution of a short pulse.

2.1. Pulse compression using binary phase coding (BPC)

We used binary codes to produce range-Doppler images of the asteroid at both Arecibo and Goldstone. In this technique we modulated the transmitted carrier with a repeating pseudo-random code using binary phase shift keying (BPSK). The duration of the code is called the pulse repetition period (PRP). The effective bandwidth of the transmitted signal (B_{eff}) is given by $1/T_{\text{baud}}$, where T_{baud} is the duration of each symbol of the code. For each run we transmitted for approximately the RTT to the asteroid, followed by reception for a similar duration. The received signal was demodulated and then decoded by cross-correlating it with a replica of the transmitted code. The images span a range (Δr) given by:

$$\Delta r = \frac{c}{2} \text{PRP}, \quad (3)$$

and their range resolution (δr) is given by:

$$\delta r = \frac{c}{2} T_{\text{baud}} = \frac{c}{2} \frac{1}{B_{\text{eff}}}, \quad (4)$$

where c is the speed of light. Each baud within the code eventually maps into to a particular range bin in the image. Resolution in the frequency or Doppler dimension was obtained in each range bin by performing a FFT on the sequence of returns corresponding to that bin. The total frequency extent (Δf) or bandwidth (BW) of the image is equal to the pulse repetition frequency (PRF) or the reciprocal of the PRP:

$$\Delta f = \text{PRF} = \frac{1}{\text{PRP}}. \quad (5)$$

The frequency resolution (δf) of the image depends on the FFT length (n) as follows:

$$\delta f = \frac{\Delta f}{n}. \quad (6)$$

The RTT dictates the finest frequency resolution achievable, similar to the situation with CW spectra.

2.2. Pulse compression using linear frequency modulation (Chirp)

We used a linear frequency modulation technique (Peebles 2007; Margot 2001) to produce range-Doppler images of the asteroid at Goldstone. Chirp waveforms allow us to maximize the bandwidth of the transmitted signal and to obtain better range resolution than that available with BPC waveforms. They are also less susceptible to

degradation due to the Doppler spread of the targets. Finally, they are more amenable to the application of windowing functions that can be used to trade between range resolution and range sidelobe level (Margot 2001).

In this technique the carrier was frequency modulated with a linear ramp signal. The resultant signal had a frequency that varied linearly with time from $\omega_0 - \omega$ to $\omega_0 + \omega$, where ω_0 is the carrier frequency and $B_{\text{eff}} = 2\omega$ is the effective bandwidth of the signal. The resultant signal is called a chirp. A repeating chirp was transmitted with 100% duty cycle for the duration of the round-trip light-time to the asteroid. The time interval between the transmission of two consecutive chirps is the PRP. For our observations we used PRPs of 125 μs and 50 μs for chirps with $B_{\text{eff}}=2$ MHz and $B_{\text{eff}}=5$ MHz, respectively. The received signal was demodulated and range compression was achieved by cross-correlating the echo with a replica of the transmitted signal. The range extent and the range resolution of the chirp images are given by Eq. (3) and Eq. (4), respectively. Resolution in the frequency or Doppler dimension was obtained as in the binary coding technique. The bandwidth of the image is given by Eq. (5) and the frequency resolution is given by Eq. (6).

3. ASTROMETRY AND ORBIT

A radar astrometric measurement consists of a range or Doppler estimate of hypothetical echoes from the center of mass (COM) of the object at a specified coordinated universal time (UTC). In practice we used our measurements of the position of the leading edge of the echoes and our estimates of the object’s size to report preliminary COM range estimates and uncertainties. We refined those estimates after we obtained a detailed shape model (Section 7). We measured Doppler astrometry from the CW spectra. We reported 9 range estimates and 1 Doppler estimate during the course of the observing run and computed the heliocentric orbit using the JPL on-site orbit determination software (OSOD). The ephemeris solution was updated each time new astrometric measurements were incorporated (Table 1).

At the end of our February observing campaign, we were using ephemeris solution 59. A final range measurement, obtained during the asteroid’s close approach in August 2012, was incorporated to generate orbit solution 74. After the shape model was finalized, we updated the orbit to solution 76 by replacing the preliminary February astrometric measurements with shape-based astrometric measurements. Table 2 lists the final radar astrometric measurements.

Table 3 lists the best fit orbital parameters (solution 76) generated using 18 range measurements and 316 optical measurements. The optical measurements span February 1977 to December 2012. However we assigned 20 arcsecond uncertainties to the two precovery observations from the 1977 La Silla-DSS plates, effectively removing their contribution to the fit and reducing the optical arc to the interval 2000-2012. The 1977 observations were from a single, hour-long, trailed exposure, and appear to have been reported with a ~ 45 s timing error, consistent with the measurers’ cautionary note “Start time and exposure length are uncertain” (MPEC 2000-L19).

The orbit computation is reliable over a period from

the year 460 to 2813. Beyond this interval either the 3σ uncertainty of the Earth close approach time exceeds 10 days or the 3σ uncertainty of the Earth close approach distance exceeds 0.1 AU. Here encounter distances of less than 0.1 AU are considered as close approaches. The current *Minimum Orbit Intersection Distance* (MOID) with respect to Earth is 0.03154 AU, making 2000 ET70 a potentially hazardous asteroid (PHA).

4. RADAR SCATTERING PROPERTIES

We transmitted circularly polarized waves and used two separate channels to receive echoes having the same circular (SC) and the opposite circular (OC) polarization as that of the transmitted wave (Ostro 1993). Reflections from a plane surface reverse the polarization of the incident waves and most of the echo power is expected in the OC polarization. Echo power in the SC polarization is due to multiple reflections or reflections from structures with wavelength-scale roughness at the surface or sub-surface. A higher ratio of SC to OC power therefore indicates a greater degree of near-surface wavelength-scale roughness or multiple scattering. This *circular polarization ratio* is often denoted by μ_C . We measured μ_C for all the Arecibo spectra shown in Fig. 2 and computed an average value of $\mu_C = 0.21 \pm 0.02$, where the error bar is the standard deviation of the individual estimates. Observed ratios for individual spectra deviate no more than 0.03 from the average. This ratio is lower than that for the majority of NEAs with known circular polarization ratios (Benner et al. 2008) suggesting that 2000 ET70 has a lower than average near-surface roughness at 10 cm scales.

In our modeling of the shape of the asteroid (Sections 6 and 7), we used a cosine law to represent the radar scattering properties of 2000 ET70:

$$\frac{d\sigma}{dA} = R(C + 1)(\cos \alpha)^{2C}. \quad (7)$$

Here σ is the radar cross section, A is the target surface area, R is the Fresnel reflectivity, C is a parameter describing the wavelength-scale roughness, and α is the incidence angle. C is related to the wavelength-scale adirectional root-mean-square (RMS) slope S_0 and angle θ_{rms} of the surface by $S_0 = \tan(\theta_{\text{rms}}) = C^{-1/2}$. Larger values of C represent more specular scattering (Mitchell et al. 1996).

5. RANGE AND DOPPLER EXTENTS

The range extent of the object in the radar images varies between ~ 600 m and ~ 1700 m (Fig. 8), suggesting that the asteroid is significantly elongated. In most of the images two distinct ridges that surround a concavity are clearly visible (e.g., Fig. 8, images 8-12 and images 30-37). In images where the ridges are aligned with the Doppler axis, they span almost the entire bandwidth extent of the asteroid (e.g., Fig. 8, images 11 and 34). If the concavity is a crater then these ridges could mark its rim. At particular viewing geometries, the trailing end of the asteroid exhibits a large outcrop with a range extent of ~ 250 m (e.g., Fig. 8, images 11). These features suggest that the overall surface of the asteroid is highly irregular at scales of hundreds of meters.

For a spherical object, the bandwidth (B) of the radar

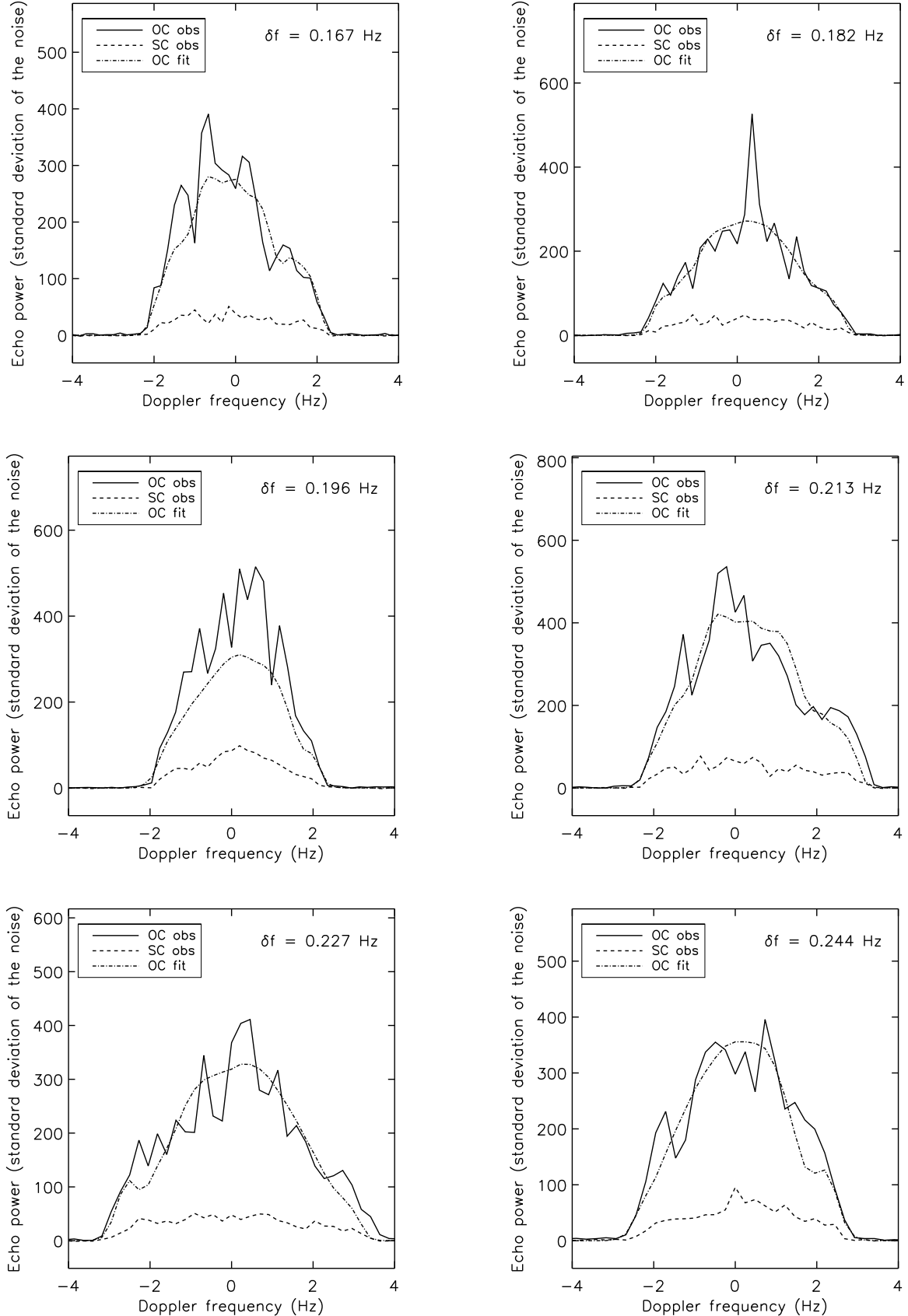


FIG. 2.— Arecibo CW spectra of 2000 ET70 arranged in chronological order from left to right and top to bottom. They were obtained on February 12-17 (MJDs 55969.35, 55970.34, 55971.33, 55972.32, 55973.32, 55974.32, respectively). The frequency resolution of each spectrum is given at the top right of the corresponding panel. Each spectrum was produced by choosing a frequency resolution that allowed for the incoherent sum of 10 independent spectra, or *looks*, per run, and by summing over 3 runs, resulting in a total number of 30 looks. The solid and dashed lines are observed OC and SC spectra, respectively. The dot-dashed line shows the corresponding synthetic OC spectra generated using our shape model (Section 7). The circular polarization ratio (μ_C) values in chronological order are 0.18, 0.20, 0.24, 0.21, 0.21, and 0.24 all of which have uncertainties of 5%, where the uncertainty is computed according to Ostro et al. (1983).

TABLE 2
RADAR ASTROMETRIC MEASUREMENTS OF 2000 ET70

Date (UTC) yyyy-mm-dd hh:mm:ss	Range μs	1- σ Uncertainty μs	Observatory
2012-02-12 08:50:00	67220894.76	0.5	A
2012-02-12 10:03:00	66974197.50	0.5	A
2012-02-13 09:11:00	62452848.06	0.5	A
2012-02-13 10:00:00	62298918.42	0.5	A
2012-02-14 09:28:00	58061903.74	0.5	A
2012-02-14 10:06:00	57953990.18	0.5	A
2012-02-14 10:16:00	57925824.25	0.5	A
2012-02-15 08:30:00	54319877.92	0.5	A
2012-02-15 09:20:00	54206358.81	3.0	G
2012-02-15 09:47:00	54126135.16	0.5	A
2012-02-16 08:23:00	50979848.61	0.5	A
2012-02-16 09:30:00	50840187.02	0.5	A
2012-02-17 08:05:00	48327621.88	0.5	A
2012-02-17 08:43:00	48267222.55	0.5	A
2012-02-18 07:40:00	46481930.28	2.0	G
2012-02-19 07:30:00	45481292.56	2.0	G
2012-02-20 10:10:00	45483470.81	2.0	G
2012-08-24 17:08:00	153139162.28	3.0	A

NOTE. — The first column indicates the coordinated universal time (UTC) of the measurement epoch. The second column gives the range measurements as the RTT to the asteroid in microseconds (μs). The third column lists the 1σ range uncertainty. The fourth column indicates the radar used to make the measurement (A stands for the Arecibo Planetary Radar and G stands for the Goldstone Solar System Radar at DSS-14).

TABLE 3

2000 ET70 HELIOCENTRIC ORBITAL ELEMENTS (SOLUTION 76)

Element	Value	1- σ Uncertainty
eccentricity	0.123620379	6.3×10^{-8}
semi-major axis (AU)	0.9466347364	1.2×10^{-9}
inclination (degrees)	22.3232174	1.2×10^{-6}
longitude of ascending node (degrees)	331.16730395	9.8×10^{-7}
argument of perihelion (degrees)	46.106698	1.1×10^{-5}
Mean anomaly (degrees)	84.37370818	4.2×10^{-7}

NOTE. — All orbital elements are specified at epoch 2012 Dec 15.0 barycentric dynamical time (TDB) in the heliocentric ecliptic reference frame of J2000. The corresponding orbital period is $(336.41246710 \pm 5.5 \times 10^{-7})$ days.

echo is given by:

$$B = \frac{4\pi D}{\lambda P} \cos \delta. \quad (8)$$

Here D is the diameter of the object, P is its apparent spin period, λ is the radar wavelength, and δ is the sub-radar latitude. As δ increases, B decreases. In images obtained at similar rotational phases, the bandwidth extent of the asteroid increased from February 12 to 20, indicating that our view was more equatorial towards the end of the observing campaign (Fig. 1). For example in Fig. 8, images 10, 33, and 68 are at similar rotational phases and their bandwidths are ~ 3.7 Hz, ~ 4.9 Hz, and 6.3 Hz, respectively.

6. SPIN VECTOR

We used the SHAPE software (Hudson 1993; Magri et al. 2007) to fit a shape model to the radar images and to estimate the spin vector of 2000 ET70. Since SHAPE is not particularly effective at fitting the spin axis orientation and spin period of the shape model, we carried out an extensive search for these parameters in an iterative manner. We performed two iterations each in our search for the spin axis orientation and spin period.

Our initial estimate of the spin period came from the time interval between repeating rotational phases of the object captured in the images. Fig. 3 shows the object at similar orientations in images taken on different days. The time interval in two of those cases is ~ 72 hours and in the third case is ~ 45 hours. This indicates that the spin period of the object is close to a common factor of the two, that is, 9 hours or a sub-multiple of 9 hours. Fig. 4 shows two images taken 22.5 hours apart and the object is not close to similar orientations in these two images, ruling out all periods that are factors of 22.5 hours. Thus we are left with a period close to 9 hours.

Using an initially fixed spin period of 9 hours, we performed an extensive search for the spin axis orientation. The search consisted of fitting shape models to the images under various assumptions for the spin axis orientation. We covered the entire celestial sphere with uni-

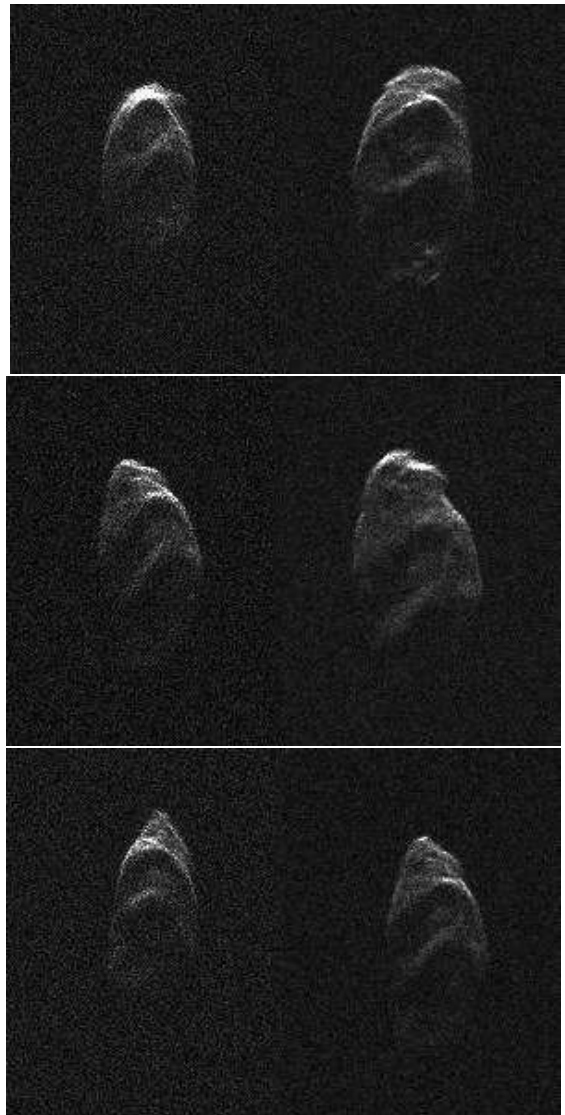


FIG. 3.— 2000 ET70 range-Doppler images showing the asteroid at similar rotational phases on different days. The images were obtained at MJDs 55970.40 and 55973.38 (~ 72 hours apart) (top), 55971.35 and 55974.33 (~ 72 hours apart) (center), 55969.46 and 55971.34 (~ 45 hours apart) (bottom), suggesting a spin period of ~ 9 hours or a sub-multiple of ~ 9 hours. In these images radar illumination is from the top, range increases towards the bottom, Doppler frequency increases to the right, and the asteroid spin results in counter-clockwise rotation.

form angular separations of 15° between neighboring trial poles. At this stage we used a subset of the images in order to decrease the computational burden. We chose images showing sharp features that repeated on different days because they provide good constraints on the spin state. Images obtained on February 12 and 15 satisfied these criteria and we used images with receive times spanning MJDs 55969.426 to 55969.463 and 55972.335 to 55972.423 for this search. We started with triaxial ellipsoid shapes and allowed the least-squares fitting procedure to adjust all three ellipsoid dimensions in order to provide the best match between model and images. We then used shapes defined by a vertex model with 500 vertices and 996 triangular facets. The fitting procedure was allowed to adjust the positions of the vertices to minimize the misfit. In all of these fits the spin axis



FIG. 4.— 2000 ET70 images obtained at MJDs 55970.40 and 55971.34, or 22.5 hours apart. The asteroid is not close to similar rotational phases in these images, ruling out spin periods that are sub-multiples of ~ 22.5 hours. A ~ 4.5 -hour spin period is therefore ruled out, leaving ~ 9 hours as the only plausible value.

orientation and the spin rate were held constant. Radar scattering parameters R and C described in Eq. (7) were allowed to float. We found the best shape model fit with the spin pole at ecliptic longitude (λ) = 60° and ecliptic latitude (β) = -60° .

Using the best fit spin pole from the previous step, we proceeded to estimate the spin period with greater precision. We tried spin rates in increments of $2^\circ/\text{day}$ from $960^\circ/\text{day}$ ($P = 9$ hours) to $970^\circ/\text{day}$ ($P = 8.91$ hours) to fit vertex shape models with 500 vertices to the images. This time we used a more extensive dataset consisting of all images obtained from Arecibo. As in the previous step, only the radar scattering parameters and the shape parameters were allowed to float in addition to the parameter of interest. We found the best agreement between model and observations with a spin rate of $964^\circ/\text{day}$ (Period = 8.963 hours).

The second iteration of the spin-axis orientation search was similar to the first one except that we used a spin period of 8.963 hours and used the complete dataset consisting of all the Arecibo and Goldstone images from February. The Arecibo images from August were not used because of their low SNR and resolution. This procedure was very effective in constraining the possible spin axis orientations to a small region of the celestial sphere (Fig. 5). We performed a higher resolution search within this region with spin poles ranging in λ from 64° to 104° and β from 30° to 60° with step sizes of 4° in λ and 5° in β . For this step we performed triaxial ellipsoid fits followed by spherical harmonics model fits, adjusting spherical harmonic coefficients up to degree and order 10. Our best estimate of the spin axis orientation is $\lambda = 80^\circ$ and $\beta = -50^\circ$, with 10° uncertainties. Shape models with spin axis orientations within this region have similar appearance upon visual inspection. We also attempted shape model fits with the best-fit prograde pole at $\lambda = 232^\circ$ and $\beta = 75^\circ$. We found that we were unable to match the observed bandwidths and ruled out the prograde solution. 2000 ET70 is a retrograde spinner, just like the majority of NEAs (La Spina et al. 2004). Our adopted spin pole ($\lambda = 80^\circ$, $\beta = -50^\circ$) is at an angle of $\sim 160^\circ$ from the heliocentric orbit pole ($\lambda = 241^\circ$, $\beta = 68^\circ$).

We used the best spherical harmonics shape model from the previous search to perform a second iteration

of the spin period search. This time we fit spherical harmonics shape models using spin periods in increments of 0.001 hours from 8.940 hours to 8.980 hours. The reduced chi-squares of the shape models are shown in Fig. 6. We visually verified the quality of the fits and adopted a spin period of 8.960 ± 0.02 hours. The assigned uncertainty is conservative because a 0.02 hour difference in spin period amounts to an easily detectable $\sim 25^\circ$ offset in rotational phase over the primary observing window.

7. SHAPE MODEL

As a starting point for our final shape modeling efforts we used the results of the spin state determination (Section 6), specifically the best-fit spherical harmonics shape model with a spin period of 8.960 hours and a spin pole at $\lambda = 80^\circ$ and $\beta = -50^\circ$. We proceeded to fit all the radar images obtained in February and OC CW spectra from Fig. 2 with a vertex model having 2000 vertices and 3996 facets. At this step the vertex locations and the radar scattering parameters were fit for, but the spin vector was held fixed. We minimized an objective function that consists of the sum of squares of residuals between model and actual images, plus a number of weighted penalty functions designed to favor models with uniform density, principal axis rotation, and a reasonably smooth surface (Hudson 1993; Magri et al. 2007). The choice of weights in the penalty function is subjective, so the shape model solution is not unique. We tried to restrict the weights to the minimum value at which the penalty functions were effective. The minimization procedure with our choice of penalty functions produced a detailed shape model for 2000 ET70 (Fig. 7 and Table 4). The agreement between model and data is generally excellent (Fig. 8 and Fig. 2). The overall shape is roughly a triaxial ellipsoid with extents along the principal axes of ~ 2.61 km, ~ 2.22 km, and ~ 2.04 km, which are roughly the same as the *dynamically equivalent equal volume ellipsoid* (DEEVE) dimensions listed in table 4.

The region around the north pole has two ridges that are 1-1.5 km in length and almost 100 m higher than their surroundings. These ridges enclose a concavity that seems more asymmetric than most impact craters. Along the negative x-axis a large protrusion is visible. Such a feature could arise if the asteroid were made up of multiple large components resting on each other.

For this shape model, the best fit values for the radar scattering parameters, R and C , were 1.9 and 1.4, respectively (section 4).

8. GRAVITATIONAL ENVIRONMENT

We used our best-fit shape model and a uniform density assumption of 2000 kg m^{-3} , a reasonable density for rubble-pile NEAs, (e.g., Ostro et al. 2006), to compute the gravity field at the surface of the asteroid (Werner and Scheeres 1997). The acceleration on the surface is the sum of the gravitational acceleration due to the asteroid's mass and the centrifugal acceleration due to the asteroid's spin. An acceleration vector was computed at the center of each facet. Fig. 9 shows the variation of the magnitude of this acceleration over the surface of the asteroid. The acceleration on the surface varies between 0.54 mm s^{-2} to 0.64 mm s^{-2} , which is 4 orders of magnitude smaller than that experienced on Earth and 2 orders of magnitude smaller than that on Vesta. Cen-

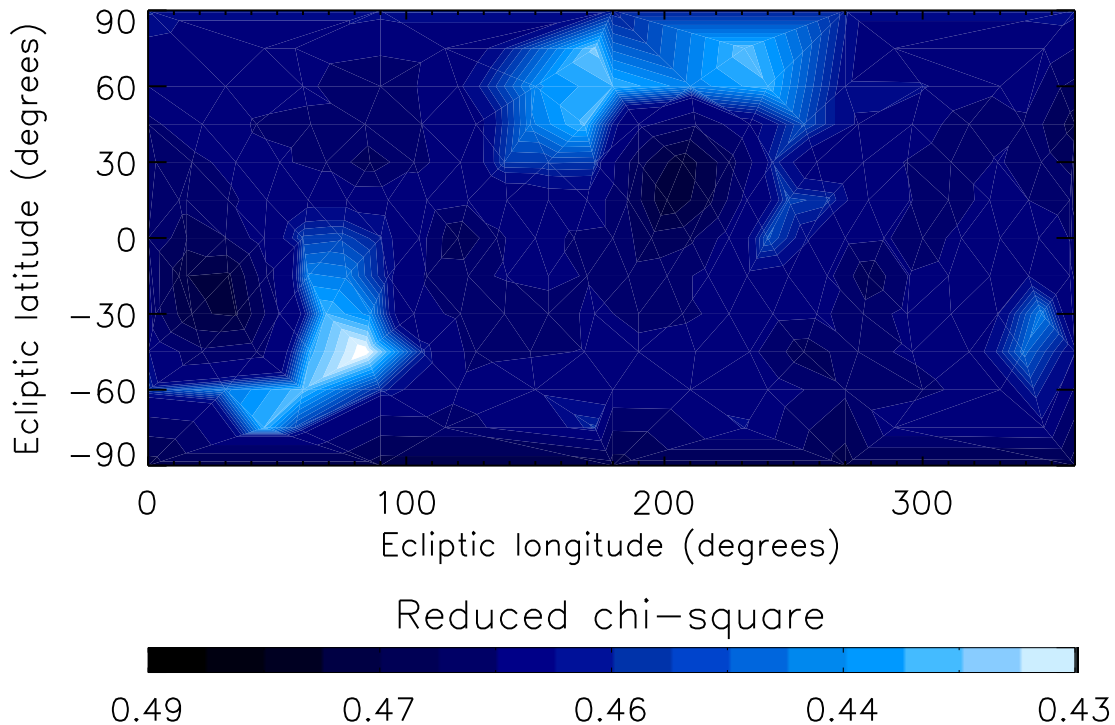


FIG. 5.— Contour plot showing goodness of fit (reduced chi-square) of shape model fits under various assumptions for the ecliptic longitude (λ) and ecliptic latitude (β) of the spin axis. We adopted a best fit spin axis orientation of $\lambda = 80^\circ$ and $\beta = -50^\circ$ with a 10° uncertainty.

TABLE 4
2000 ET70 SHAPE MODEL PARAMETERS

Parameters		Value
Extents along principal axes (km)	x	$2.614 \pm 5\%$
	y	$2.222 \pm 5\%$
	z	$2.041 \pm 5\%$
Surface Area (km ²)		$16.68 \pm 10\%$
Volume (km ³)		$6.065 \pm 15\%$
Moment of inertia ratios	A/C	$0.800 \pm 10\%$
	B/C	$0.956 \pm 10\%$
Equivalent diameter (km)		$2.262 \pm 5\%$
DEEVE extents (km)	x	$2.560 \pm 5\%$
	y	$2.187 \pm 5\%$
	z	$2.069 \pm 5\%$
Spin pole (λ, β) ($^\circ$)		$(80, -50) \pm 10$

NOTE. — The shape model consists of 2000 vertices and 3996 triangular facets, corresponding to an effective surface resolution of ~ 100 m. The moment of inertia ratios were calculated assuming homogeneous density. Here A , B , and C are the principal moments of inertia, such that $A < B < C$. Equivalent diameter is the diameter of a sphere having the same volume as that of the shape model. A *dynamically equivalent equal volume ellipsoid* (DEEVE) is an ellipsoid with uniform density having the same volume and moment of inertia ratios as the shape model.

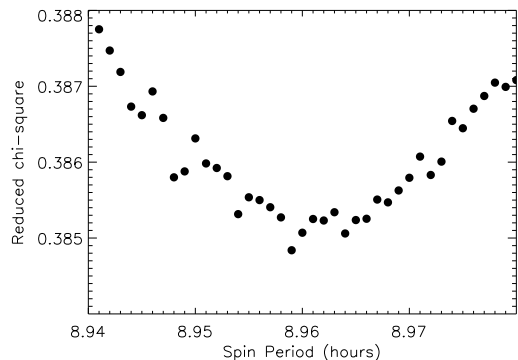


FIG. 6.— Goodness of fit (reduced chi-square) of degree-and-order 10 spherical harmonics shape models of 2000 ET70 as a function of assumed spin period. We adopted a best fit spin period of 8.960 ± 0.02 hours.

trifugal acceleration makes a significant contribution to the total acceleration and varies from zero at the poles to $\sim 0.049 \text{ mm s}^{-2}$ (about 10% of the total acceleration) on the most protruding regions of the equator. For comparison, on Earth, centrifugal acceleration contributes less than 0.5% to the total acceleration at the equator.

Fig. 10 shows the gravitational slope variation over the asteroid's surface. The gravitational slope is the angle that the local gravitational acceleration vector makes with the inward pointing surface-normal vector. The average slope is 9.5° and it reaches up to $\sim 33^\circ$ on the sides of the ridges at the north pole. The sides of the ridges facing the north pole are steeper than the opposite sides.

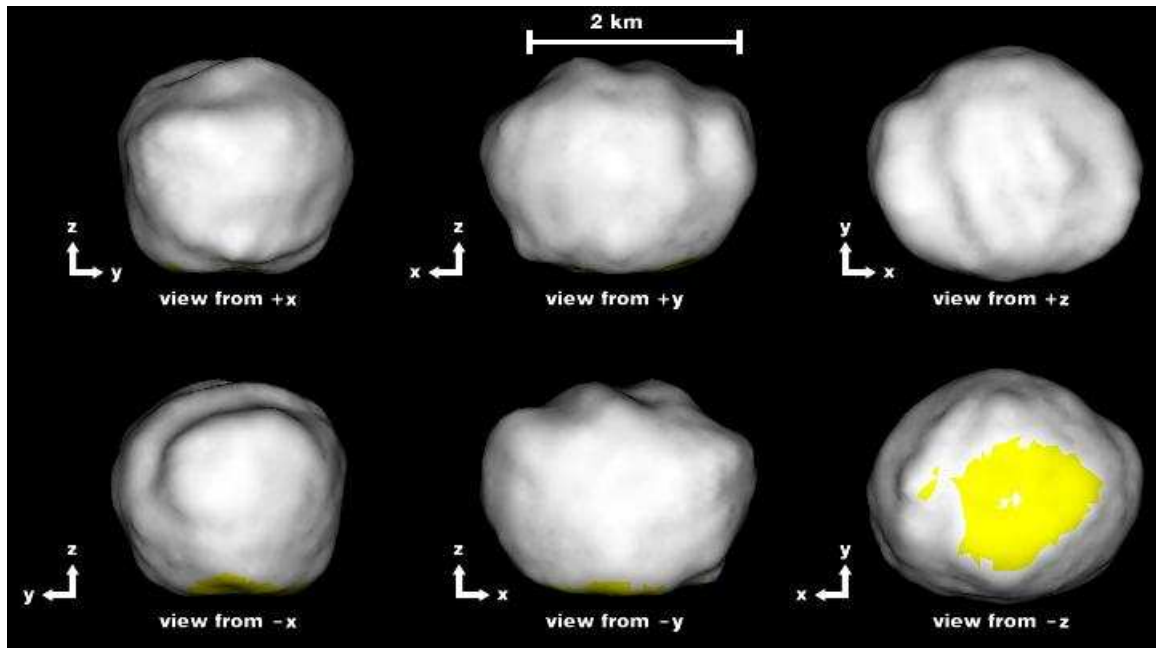


FIG. 7.— Best-fit vertex shape model of 2000 ET70 as seen along the three principal axes x , y , and z . For principal axis rotation the spin axis is aligned with the z axis. Yellow regions at the south pole have radar incidence angles $> 60^\circ$ and hence are not well constrained. The shape model has 2000 vertices and 3996 triangular facets giving an effective surface resolution of ~ 100 m.

Less than 1% of the surface has slopes greater than 30° , the approximate angle of repose of sand, indicating a relaxed surface. The regions near the north pole where the slopes are the highest may be composed of competent rocks exposed at the surface. Along-the-surface accelerations on the sides of the ridges are as high as 0.34 mm s^{-2} , so one might expect to see accumulated debris in the valley between the two ridges.

9. DISCUSSION

Whiteley (2001) estimated 2000 ET70’s absolute magnitude (H) to be 18.2. The geometric albedo (p_V) of an asteroid is related to its effective diameter (D) and its H value by (Pravec and Harris 2007):

$$p_V = \left[\frac{1329 \text{ km} \times 10^{-0.2H}}{D} \right]^2. \quad (9)$$

Using Whiteley (2001)’s $H=18.2$, the above equation yields $p_V=0.019\pm 0.002$ for an asteroid with an effective diameter of $2.2 \text{ km} \pm 6\%$ (Fig. 11). This uncertainty on p_V is due to the diameter uncertainty only as no uncertainties on H were quoted in Whiteley (2001). Although $p_V = 0.019$ is possible, it seems unreasonably low compared to the albedos of other NEAs (Thomas et al. 2011; Stuart and Binzel 2004). More common values of p_V would require lower values of the absolute magnitude (e.g., $p_V=0.04$ requires $H=17.5$). The range of possible H and p_V values that are consistent with the radar size estimates is shown in Fig. 11.

Alvarez et al. (2012) observed the asteroid between February 19 to 24, when the view was close to the equator, and reported a lightcurve amplitude of 0.60 ± 0.07 mag. If the asteroid was approximated by a triaxial ellipsoid with uniform albedo, this amplitude would suggest an elongation (ratio of equatorial axes) approximately between 1.28 and 1.36. Our shape model indicates that this ratio is ~ 1.18 , suggesting that either the ellipsoid ap-

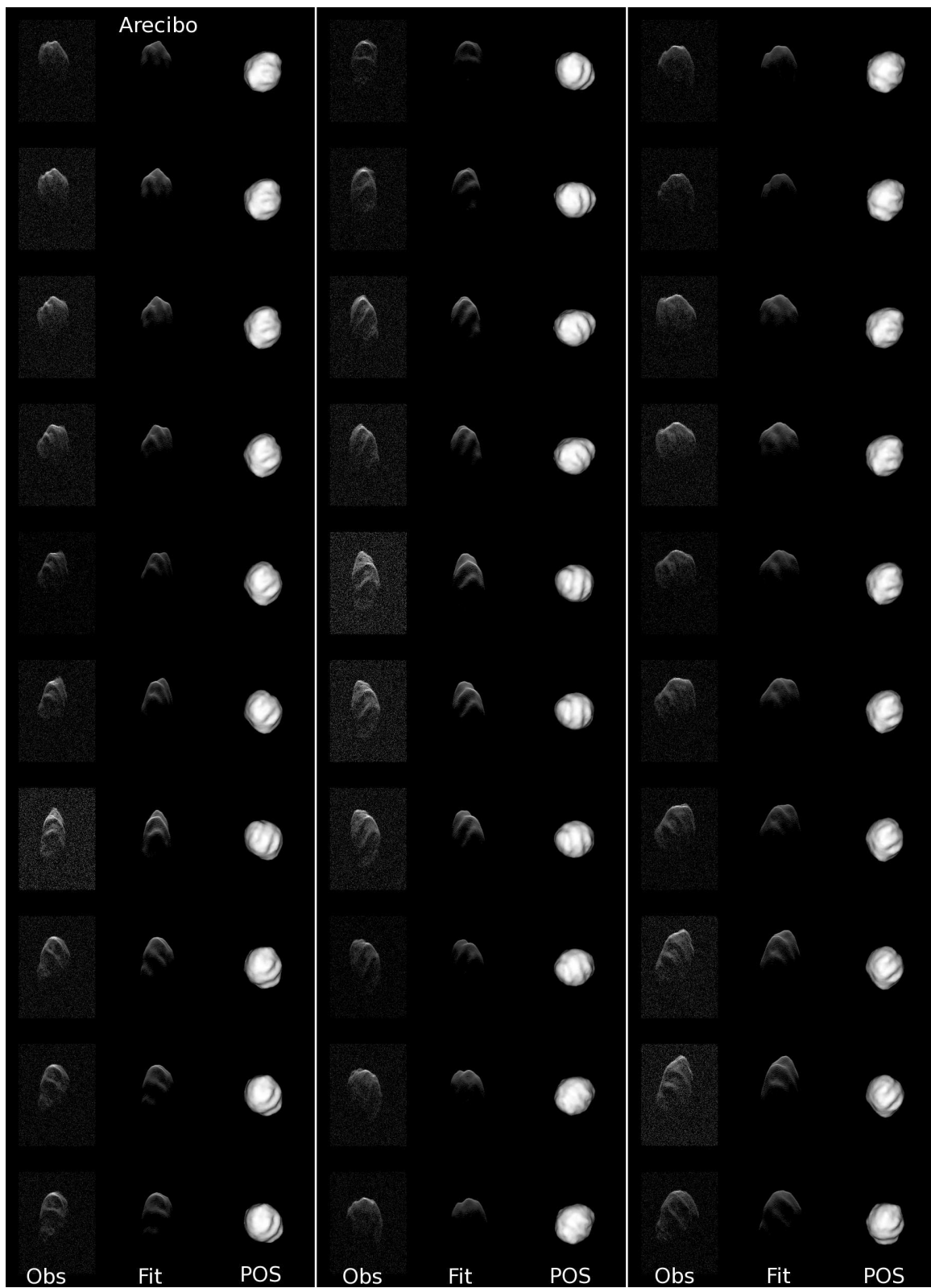
proximation is poor, the lightcurve amplitude is on the lower end of the range above, shadowing due to the terrain is playing an important role, there are albedo variations over the surface of the asteroid, or a combination of these factors.

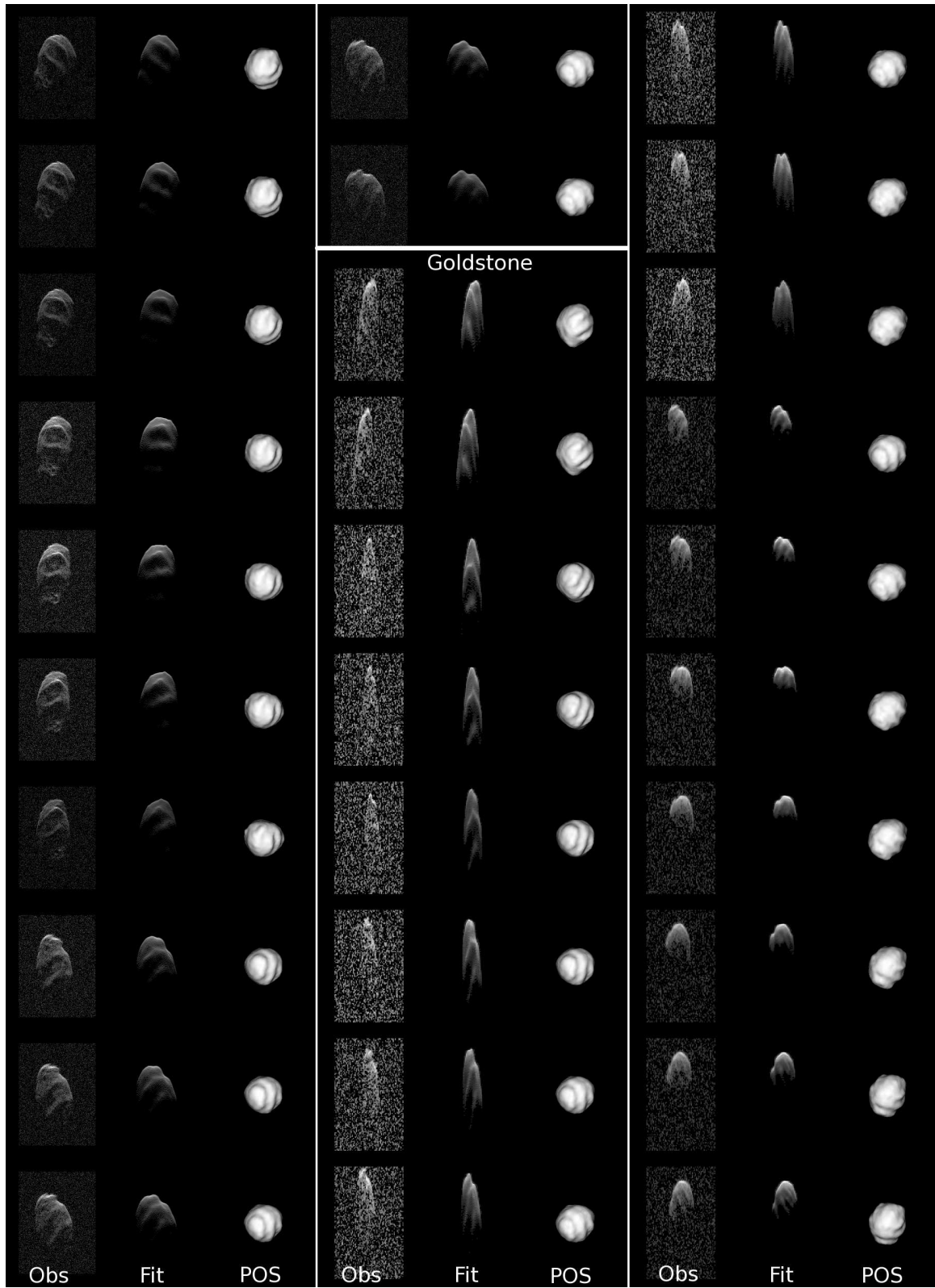
Alvarez et al. (2012) also report a period of 8.947 ± 0.001 hours, which they refer to as the “synodic period”, and which we refer to as the “lightcurve period”. The latter is a function of the intrinsic spin state of the asteroid and of the relative motion between the asteroid, the observer, and the Sun. Our shape modeling process relies on the intrinsic or sidereal period of the asteroid, which we estimate to be 8.960 ± 0.02 hours. This value can be used with our best-fit spin axis orientation and ephemerides to evaluate what we refer to as the “synodic period”, i.e., the period that combines the (fixed) intrinsic rotation and the (variable) apparent rotation due to sky motion, irrespective of the position of the Sun. On Feb 19.0, the nominal synodic period was 8.937 hours, whereas on Feb 25.0, the nominal synodic period was 8.943 hours. These synodic periods are close to the reported lightcurve period, but cannot be directly compared to it as they measure slightly different phenomena.

Arecibo and Goldstone radar observations of 2000 ET70 allowed us to provide a detailed characterization of a potentially hazardous asteroid, including its size, shape, spin state, scattering properties, and gravitational environment. These techniques are applicable to a substantial fraction of known NEAs that make close approaches to Earth within ~ 0.1 AU. Radar-based physical properties for this and other asteroids are available at <http://radarastronomy.org>.

ACKNOWLEDGMENTS

We thank the staff at Arecibo and Goldstone for assistance with the observations. The Arecibo Observatory is operated by SRI International under coopera-





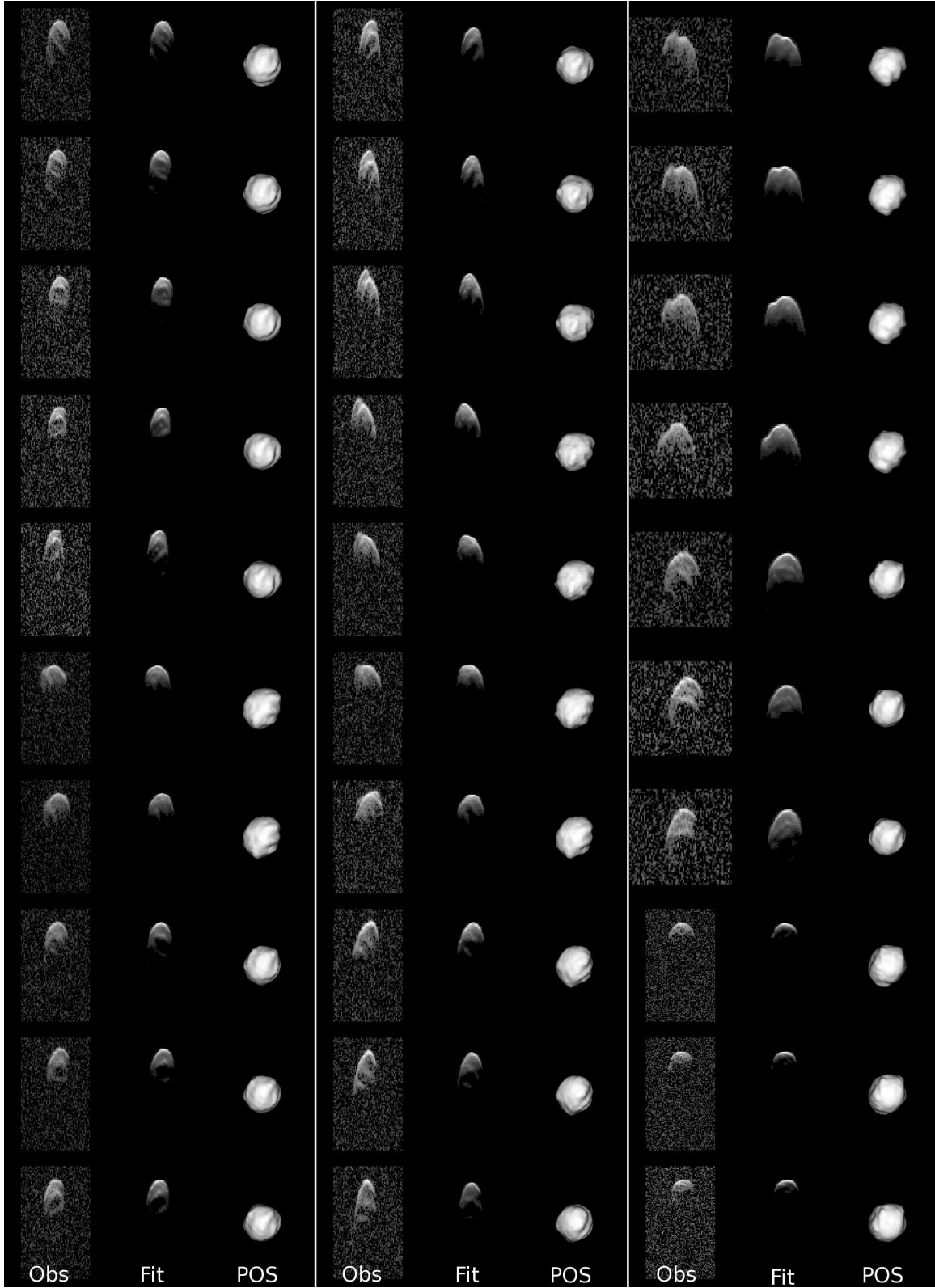


FIG. 8.— Comparison between radar range-Doppler images, corresponding synthetic radar images generated using our best-fit shape model, and plane-of-sky (POS) projections of the shape model. Range-Doppler images are oriented as in Fig. 3, and the POS projections are oriented north-up. Time increases from top to bottom within each panel and from left to right. The spatial resolution of the images is given in Table 1.

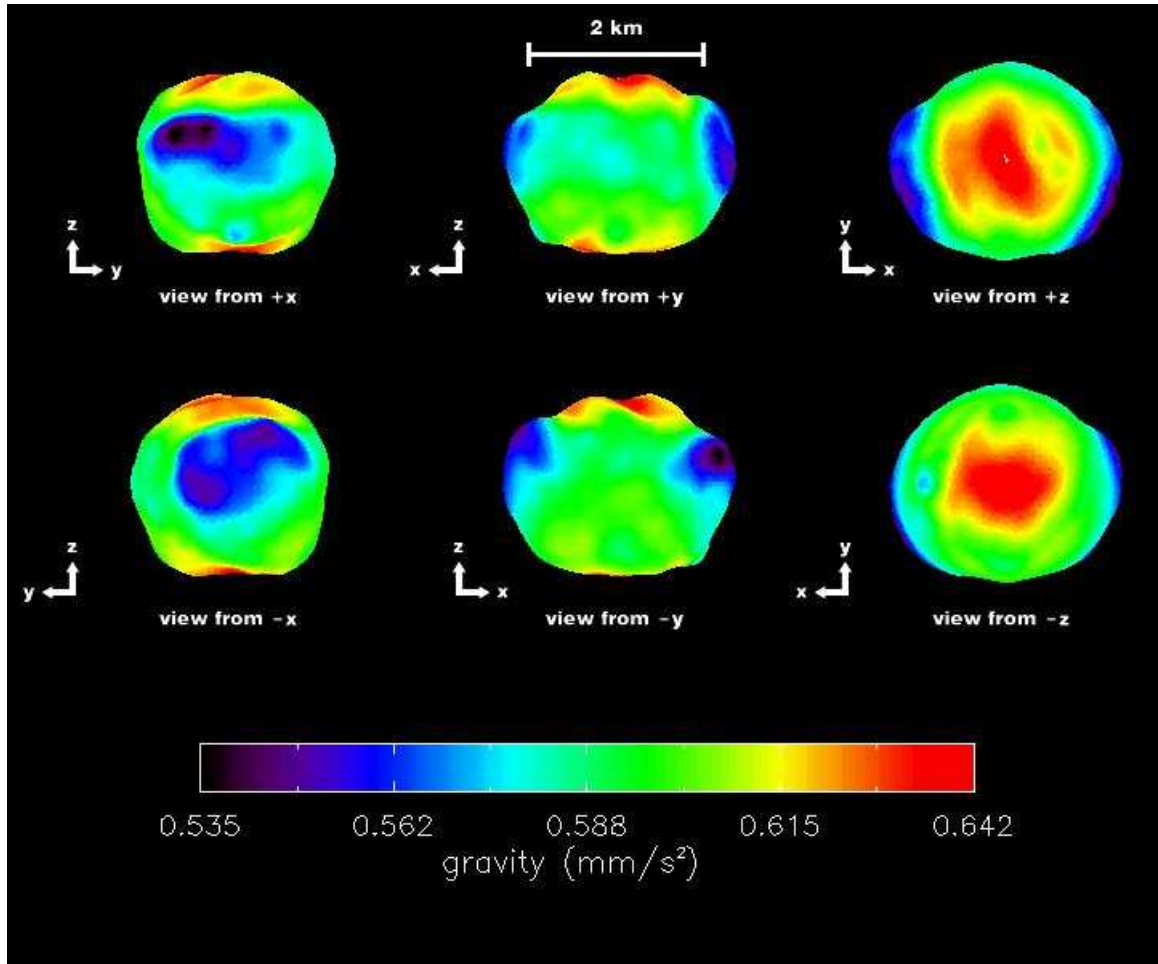


FIG. 9.— This figure shows the magnitude of the vector sum of acceleration due to gravity and centrifugal acceleration computed at the center of each facet of the shape model. We assumed a uniform density of 2000 kg m^{-3} and used our measured spin period value of 8.96 hours.

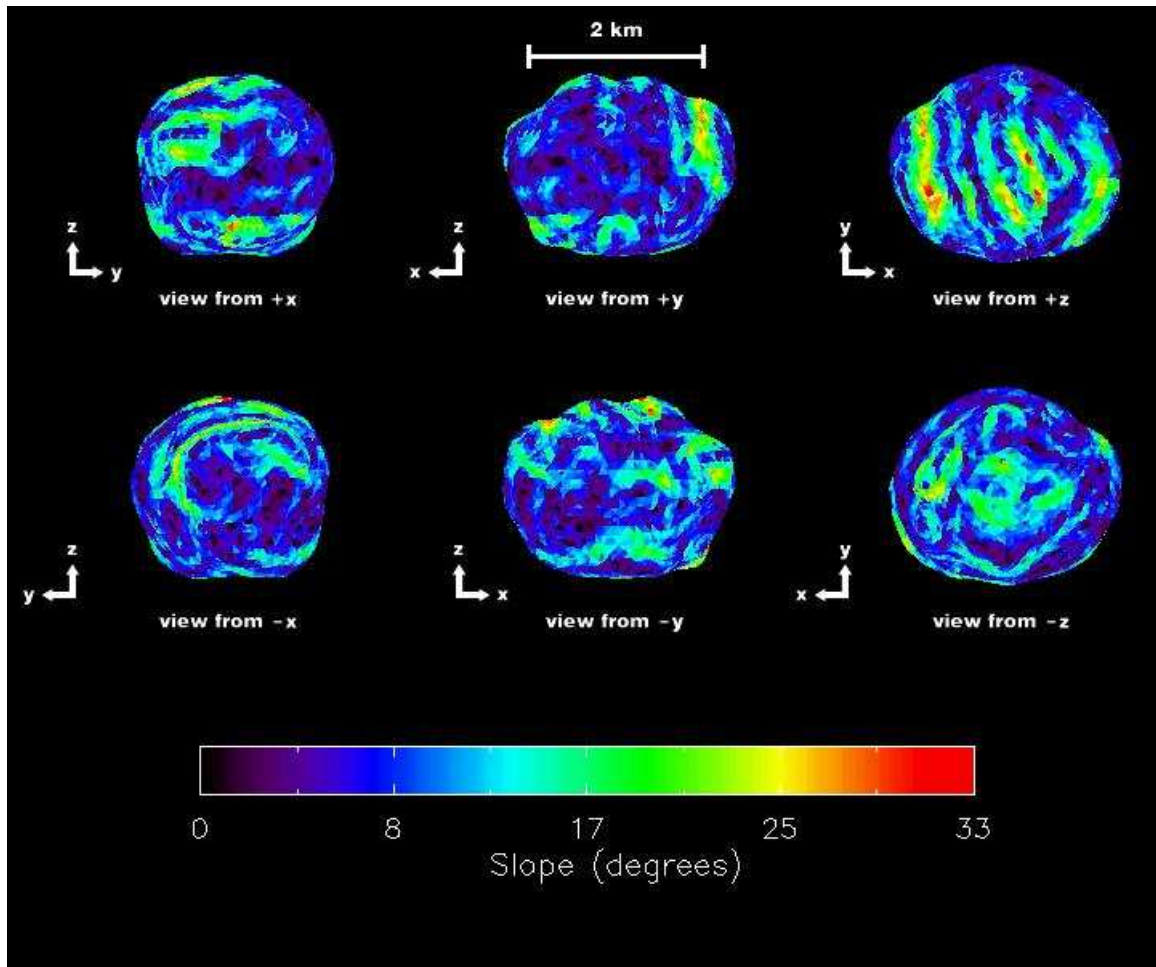


FIG. 10.— This figure shows the gravitational slopes computed at the center of each facet of the shape model. We assumed a uniform density of 2000 kg m^{-3} and used our measured spin period value of 8.96 hours.

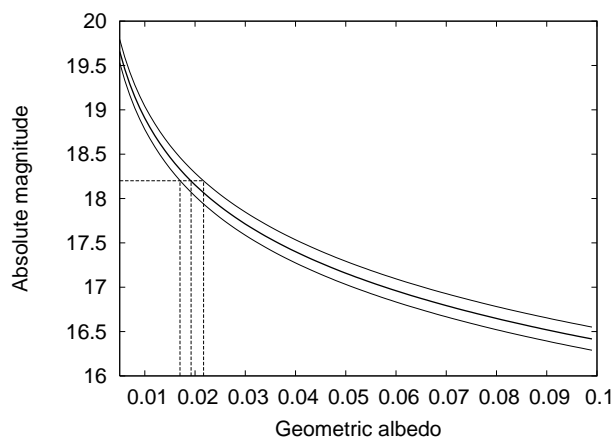


FIG. 11.— Absolute magnitude vs. geometric albedo for an effective diameter of 2.2 km (dark line) and a diameter uncertainty of 6% (light lines). The horizontal dashed line corresponds to the absolute magnitude ($H=18.2$) reported by Whiteley (2001), and the vertical dashed lines indicate the corresponding geometric albedos. These albedo values are unusually low, suggesting an extraordinarily dark object or an error in the reported H value.

agreement AST-1100968 with the National Science Foundation (NSF), and in alliance with Ana G. Méndez-Universidad Metropolitana, and the Universities Space Research Association. Some of this work was performed at the Jet Propulsion Laboratory, which is managed by the California Institute of Technology under contract with the National Aeronautics and Space Administra-

REFERENCES

- E. M. Alvarez, J. Oey, X. L. Han, O. R. Hefner, A. W. Kidd, B. J. Magetta, and F. W. Rastede. Period Determination for NEA (162421) 2000 ET70. *Minor Planet Bulletin*, 39:170, July 2012.
- L. A. M. Benner, S. J. Ostro, M. C. Nolan, J. L. Margot, J. D. Giorgini, R. S. Hudson, R. F. Jurgens, M. A. Slade, E. S. Howell, D. B. Campbell, and D. K. Yeomans. Radar observations of asteroid 1999 JM8. *Meteoritics and Planetary Science*, 37:779–792, June 2002.

- L. A. M. Benner, M. C. Nolan, S. J. Ostro, J. D. Giorgini, D. P. Pray, A. W. Harris, C. Magri, and J. L. Margot. Near-Earth Asteroid 2005 CR37: Radar images and photometry of a candidate contact binary. *Icarus*, 182:474–481, June 2006.
- L. A. M. Benner, S. J. Ostro, C. Magri, M. C. Nolan, E. S. Howell, J. D. Giorgini, R. F. Jurgens, J. L. Margot, P. A. Taylor, M. W. Busch, and M. K. Shepard. Near-Earth asteroid surface roughness depends on compositional class. *Icarus*, 198:294–304, December 2008. doi:10.1016/j.icarus.2008.06.010.
- M. Brozovic, L. A. M. Benner, C. Magri, S. J. Ostro, D. J. Scheeres, J. D. Giorgini, M. C. Nolan, J. L. Margot, R. F. Jurgens, and R. Rose. Radar observations and a physical model of contact binary Asteroid 4486 Mithra. *Icarus*, 208:207–220, July 2010.
- M. Brozović, L. A. M. Benner, P. A. Taylor, M. C. Nolan, E. S. Howell, C. Magri, D. J. Scheeres, J. D. Giorgini, J. T. Pollock, P. Pravec, A. Galád, J. Fang, J. L. Margot, M. W. Busch, M. K. Shepard, D. E. Reichart, K. M. Ivarsen, J. B. Haislip, A. P. Lacluyze, J. Jao, M. A. Slade, K. J. Lawrence, and M. D. Hicks. Radar and optical observations and physical modeling of triple near-Earth Asteroid (136617) 1994 CC. *Icarus*, 216:241–256, November 2011.
- S. R. Chesley, S. J. Ostro, D. Vokrouhlický, D. Čapek, J. D. Giorgini, M. C. Nolan, J. L. Margot, A. A. Hine, L. A. M. Benner, and A. B. Chamberlin. Direct Detection of the Yarkovsky Effect by Radar Ranging to Asteroid 6489 Golevka. *Science*, 302:1739–1742, December 2003.
- F. E. DeMeo, R. P. Binzel, S. M. Slivan, and S. J. Bus. An extension of the Bus asteroid taxonomy into the near-infrared. *Icarus*, 202:160–180, July 2009. doi:10.1016/j.icarus.2009.02.005.
- J. Fang and J. L. Margot. Near-Earth Binaries and Triples: Origin and Evolution of Spin-Orbital Properties. *AJ*, 143:24, January 2012. doi:10.1088/0004-6256/143/1/24.
- J. Fang, J. L. Margot, M. Brozovic, M. C. Nolan, L. A. M. Benner, and P. A. Taylor. Orbits of Near-Earth Asteroid Triples 2001 SN263 and 1994 CC: Properties, Origin, and Evolution. *AJ*, 141:154–+, May 2011.
- R.S. Hudson and S.J. Ostro. Shape of asteroid 4769 Castalia (1989 PB) from inversion of radar images. *Science*, 263:940–943, February 1994.
- S. Hudson. Three-dimensional reconstruction of asteroids from radar observations. *Remote Sensing Reviews*, 8:195–203, 1993.
- A. La Spina, P. Paolicchi, A. Kryszczyńska, and P. Pravec. Retrograde spins of near-Earth asteroids from the Yarkovsky effect. *Nature*, 428:400–401, March 2004. doi:10.1038/nature02411.
- S. C. Lowry, A. Fitzsimmons, P. Pravec, D. Vokrouhlický, H. Boehnhardt, P. A. Taylor, J. L. Margot, A. Galád, M. Irwin, J. Irwin, and P. Kusnirák. Direct Detection of the Asteroidal YORP Effect. *Science*, 316:272–, April 2007.
- C. Magri, S. J. Ostro, D. J. Scheeres, M. C. Nolan, J. D. Giorgini, L. A. M. Benner, and J. L. Margot. Radar observations and a physical model of Asteroid 1580 Betulia. *Icarus*, 186:152–177, January 2007. doi:10.1016/j.icarus.2006.08.004.
- J. L. Margot. Planetary Radar Astronomy with Linear FM (chirp) Waveforms. Arecibo technical and operations memo series 2001-09, Arecibo Observatory, 2001.
- J. L. Margot, M. C. Nolan, L. A. M. Benner, S. J. Ostro, R. F. Jurgens, J. D. Giorgini, M. A. Slade, and D. B. Campbell. Binary Asteroids in the Near-Earth Object Population. *Science*, 296:1445–1448, May 2002. doi:10.1126/science.1072094.
- D. L. Mitchell, S. J. Ostro, R. S. Hudson, K. D. Rosema, D. B. Campbell, R. Velez, J. F. Chandler, I. I. Shapiro, J. D. Giorgini, and D. K. Yeomans. Radar Observations of Asteroids 1 Ceres, 2 Pallas, and 4 Vesta. *Icarus*, 124:113–133, November 1996. doi:10.1006/icar.1996.0193.
- M. C. Nolan, E. S. Howell, T. M. Becker, C. Magri, J. D. Giorgini, and J. L. Margot. Arecibo Radar Observations of 2001 SN263: A Near-Earth Triple Asteroid System. In *Bulletin of the American Astronomical Society*, volume 40, 2008.
- C. R. Nugent, J. L. Margot, S. R. Chesley, and D. Vokrouhlický. Detection of semi-major axis drifts in 54 near-earth asteroids: New measurements of the yarkovsky effect. *Astronomical Journal*, 144:60, 2012. Arxiv eprint 1204.5990.
- S. J. Ostro. Planetary radar astronomy. *Reviews of Modern Physics*, 65:1235–1279, October 1993. doi:10.1103/RevModPhys.65.1235.
- S. J. Ostro, D. B. Campbell, and I. I. Shapiro. Radar observations of asteroid 1685 Toro. *AJ*, 88:565–576, April 1983. doi:10.1086/113345.
- S. J. Ostro, R. S. Hudson, R. F. Jurgens, K. D. Rosema, D. B. Campbell, D. K. Yeomans, J. F. Chandler, J. D. Giorgini, R. Winkler, R. Rose, S. D. Howard, M. A. Slade, P. Perillat, and I. I. Shapiro. Radar Images of Asteroid 4179 Toutatis. *Science*, 270:80–83, October 1995. doi:10.1126/science.270.5233.80.
- S. J. Ostro, J. L. Margot, L. A. M. Benner, J. D. Giorgini, D. J. Scheeres, E. G. Fahnestock, S. B. Broschart, J. Bellerose, M. C. Nolan, C. Magri, P. Pravec, P. Scheirich, R. Rose, R. F. Jurgens, E. M. De Jong, and S. Suzuki. Radar Imaging of Binary Near-Earth Asteroid (66391) 1999 KW4. *Science*, 314:1276–1280, November 2006. doi:10.1126/science.1133622.
- P.Z. Peebles. *Radar Principles*. Wiley India Pvt. Limited, 2007. ISBN 9788126515271. URL <http://books.google.com/books?id=rnX21aAMKJCIC>.
- P. Pravec and A. W. Harris. Binary asteroid population. 1. Angular momentum content. *Icarus*, 190:250–259, September 2007. doi:10.1016/j.icarus.2007.02.023.
- D. J. Scheeres, E. G. Fahnestock, S. J. Ostro, J. L. Margot, L. A. M. Benner, S. B. Broschart, J. Bellerose, J. D. Giorgini, M. C. Nolan, C. Magri, P. Pravec, P. Scheirich, R. Rose, R. F. Jurgens, E. M. De Jong, and S. Suzuki. Dynamical Configuration of Binary Near-Earth Asteroid (66391) 1999 KW4. *Science*, 314:1280–1283, November 2006. doi:10.1126/science.1133599.
- M. K. Shepard, J. L. Margot, C. Magri, M. C. Nolan, J. Schlieder, B. Estes, S. J. Bus, E. L. Volquardsen, A. S. Rivkin, L. A. M. Benner, J. D. Giorgini, S. J. Ostro, and M. W. Busch. Radar and infrared observations of binary near-Earth Asteroid 2002 CE26. *Icarus*, 184:198–210, September 2006. doi:10.1016/j.icarus.2006.04.019.
- J. S. Stuart and R. P. Binzel. Bias-corrected population, size distribution, and impact hazard for the near-Earth objects. *Icarus*, 170:295–311, August 2004. doi:10.1016/j.icarus.2004.03.018.
- P. A. Taylor and J. L. Margot. Binary asteroid systems: Tidal end states and estimates of material properties. *Icarus*, 212:661–676, April 2011.
- P. A. Taylor, J. L. Margot, D. Vokrouhlický, D. J. Scheeres, P. Pravec, S. C. Lowry, A. Fitzsimmons, M. C. Nolan, S. J. Ostro, L. A. M. Benner, J. D. Giorgini, and C. Magri. Spin Rate of Asteroid (54509) 2000 PH5 Increasing Due to the YORP Effect. *Science*, 316:274–, April 2007. doi:10.1126/science.1139038.
- D. J. Tholen. *Asteroid taxonomy from cluster analysis of Photometry*. PhD thesis, Arizona Univ., Tucson., 1984.
- C. A. Thomas, D. E. Trilling, J. P. Emery, M. Mueller, J. L. Hora, L. A. M. Benner, B. Bhattacharya, W. F. Bottke, S. Chesley, M. Delbó, G. Fazio, A. W. Harris, A. Mainzer, M. Mommert, A. Morbidelli, B. Penprase, H. A. Smith, T. B. Spahr, and J. A. Stansberry. ExploreNEOs. V. Average Albedo by Taxonomic Complex in the Near-Earth Asteroid Population. *AJ*, 142:85, September 2011. doi:10.1088/0004-6256/142/3/85.
- R. A. Werner and D. J. Scheeres. Exterior Gravitation of a Polyhedron Derived and Compared with Harmonic and Mascon Gravitation Representations of Asteroid 4769 Castalia. *Celestial Mechanics and Dynamical Astronomy*, 65:313–344, 1997.
- R. J. Whiteley, Jr. *A compositional and dynamical survey of the near-Earth asteroids*. PhD thesis, University of Hawai'i at Manoa, 2001.